Manuscript prepared for Atmos. Chem. Phys.
with version 2014/09/16 7.15 Copernicus papers of the LaTeX class copernicus.cls.
Date: 10 January 2016

Spectral Optical Layer Properties of Cirrus from Collocated Airborne Measurements and Simulations

Fanny Finger[1,5], Frank Werner[1,2], Marcus Klingebiel[3], André Ehrlich[1], Evelyn Jäkel[1], Matthias Voigt[3], Stephan Borrmann[3,4], Peter Spichtinger[3], and Manfred Wendisch[1]

[1]Leipzig Institute for Meteorology (LIM), University of Leipzig, Germany
[2]University of Maryland (UMBC), Physics Department, Baltimore, Maryland, USA
[3]Institute for Atmospheric Physics, Johannes Gutenberg University Mainz, Germany
[4]Max Planck Institute for Chemistry, Mainz, Germany
[5]Dr. Födisch Umweltmesstechnik AG, Markranstädt, Germany

Correspondence to: F. Finger
f.finger@uni-leipzig.de

Abstract. Spectral solar optical layer properties of cirrus are derived from simultaneous and vertically collocated measurements of spectral upward and downward solar irradiances above and below the cirrus layer. From the irradiance data spectral transmissivity, absorptivity, reflectivity, and cloud top albedo of the observed cirrus layer are obtained. The radiation measurements are supplemented by in–situ microphysical measurements and radiative transfer simulations based on the microphysical data. The close collocation of the radiative and microphysical measurements, above, beneath and inside the cirrus, is accomplished by using a research aircraft (Learjet 35A) in tandem with the towed sensor platform AIRTOSS (AIRcraft TOwed Sensor Shuttle). AIRTOSS can be released from and retracted back to the research aircraft by means of a cable up to a distance of 4 km. Data were collected in two field campaigns over the North Sea and the Baltic Sea in spring and late summer 2013. Exemplary results are discussed also to illustrate the benefits of collocated sampling.

Furthermore, based on the measured cirrus microphysical properties, radiative transfer simulations were applied to quantify the impact of cloud particle properties such as crystal shape, effective radius r_{eff}, and optical thickness τ on cirrus spectral optical layer properties. The effects of clouds beneath the cirrus are evaluated. They may cause changes in both the spectral optical layer properties and the radiative forcing of the cirrus by a factor of 2. If low–level clouds below the cirrus are not taken into account the solar cooling due to the cirrus is significantly overestimated.

1 Introduction

Significant uncertainties in atmospheric and climate modelling originate from the insufficient description of effects and interactions of clouds with solar and terrestrial radiation (IPCC, 2013). In particular, cirrus clouds are critical; they mostly warm but can also cool the atmosphere, depending on cloud optical properties and altitude (Lynch et al., 2002). Cirrus clouds globally occur at all latitudes and in all seasons with a mean global coverage of about 20 – 30 %. More than 70 % of cirrus are observed in the tropics (Wylie et al., 1994), forming relatively stable and long–lived cloud layers (Liou, 1986). Due to different meteorological conditions and evolution processes cirrus clouds are characterized by a wide diversity of macrophysical structures, sizes and numbers of ice particles, crystal shapes and orientations. Horizontal and vertical inhomogeneities of these properties increase the complexity of cirrus. The radiative layer properties (reflectivity, transmissivity, and absorptivity) of cirrus depend on the microphysical (effective radius r_{eff}, ice water content IWC) and optical (absorption, scattering) characteristics.

Cirrus inhomogeneities and varying crystal shapes impact (i) the energy budget of the Earth's atmosphere, and (ii) the remote sensing of cirrus optical thickness τ and r_{eff}, which is often based on one–dimensional (1D) radiative transfer modelling. Schlimme et al. (2005) found that the horizontal variability of the extinction coefficient leads to significant differences in the solar irradiance compared to a homogeneous cloud, resulting in a variability of transmittance of about 80 %. Zhang et al. (1999) reported that the radiative forcing of cirrus may switch sign depending on the geometry and size of the ice crystals. The impact of ice crystal shape on the cirrus radiative forcing, depending on the solar zenith angle, can vary between 10 and 26 % for the solar spectral range (Wendisch et al., 2005), while for the thermal infrared spectral range even differences of up to 70 % are found (Wendisch et al., 2007). Eichler et al. (2009) investigated the influence of ice crystal shape on the retrieval of τ and r_{eff} and reported effects of up to 70 % for τ and 20 % for r_{eff}.

Measurements of spectral layer properties of cirrus are rarely available. Commonly a combination of measurements and simulations is applied to derive layer properties, whereby τ and r_{eff} are retrieved from reflected radiance (airborne or space – borne) (see Francis et al., 1998) and then used in combination with a radiative transfer model to simulate layer reflectivity, transmissivity, and absorptivity.

Airborne measurements of cirrus optical layer properties are hard to obtain if only one aircraft is used. Usually, the radiative measurements above and below the cirrus are performed consecutively (e.g., Pilewskie and Valero, 1992). This method unavoidably involves a temporal shift between the two measurements above and below the cirrus and, thus, can be applied for rather static and horizontal homogeneous cloud layers only. Therefore, helicopter–borne towed platforms have been developed and adapted, such as the Airborne Cloud Turbulence Observation System (ACTOS) for microphysical in situ instruments, and the Spectral Modular Airborne Radiation measurements sysTem – HELIcopter–borne Observations of Spectral Radiation (SMART–HELIOS) for solar spectral reflectivity measurements (Henrich et al., 2010; Werner et al., 2013, 2014). For cirrus measurements, Frey et al. (2009) introduced the aircraft–borne AIRTOSS (AIRcraft TOwed Sensor Shuttle), shown in Fig. 1.

In this paper an extended version of AIRTOSS will be presented with additional spectral radiation sensors, which allows for the first time to derive cloud optical layer properties from truly collocated spectral upward and downward radiation measurements. In Section 2 the instrumentation of the aircraft and AIRTOSS is described. In particular, the solar spectral radiation instruments and their combination to derive optical layer properties are discussed in Section 3. In Section 4 the calculated solar spectral layer properties and the concurrent microphysical observations are introduced for one exemplary measurement case. Based on these data radiative transfer simulations are performed and analyzed in Section 5.

2 Instrumentation

The instruments were mounted at different positions on the aircraft, the towed platform AIRTOSS, and an additional wing pod underneath the left wing as illustrated in Fig. 2 (a). The operation of the aircraft together with the tethered AIRTOSS is certified for altitudes up to 12.5 km (the previous ceiling limitation was 7.6 km; Frey et al., 2009).

2.1 Aircraft

The applied aircraft certified for the operation of AIRTOSS is a Learjet 35A. Instruments for measurements of trace gases and water vapor are mounted inside the cabin with special inlets sampling ambient air from outside the aircraft during the flight. An upward looking radiation sensor, measuring the downward irradiance $F^{\downarrow}$ (in $\mathrm{W\,m^{-2}\,nm^{-1}}$), was mounted on the fuselage including the Spectral Modular Airborne Radiation measurement syStem (SMART) inside the aircraft, introduced by Wendisch et al. (2001), further developed by Bierwirth et al. (2009). Optical fibers connect the optical inlet with two Zeiss Spectrometers for the visible to near infrared (300 – 2200 nm) wavelength range with a resolution (Full Width at Half Maximum, FWHM) of 2 – 3 nm (visible) and 9 – 16 nm (near infrared), respectively. An active horizontal stabilization platform (Wendisch et al., 2001) was operated to assure the horizontal levelling of the upward looking optical inlet on top of the aircraft during the aircraft measurements, which is crucial for unbiased irradiance measurements. A pod mounted under the left wing of the aircraft contains another optical inlet with a pair of spectrometers, measuring the upward irradiance. A Forward Scattering Spectrometer Probe (FSSP–100), placed at the tip of the wing pod, measures the cloud particle number size distribution (size diameter range from 2 to 47 µm, Gayet et al., 2002). To correct for shattering (Korolev et al., 2013) the FSSP–100 records the individual data particle–by–particle (Field et al., 2003, 2006). The instrument was used as indicator for the time periods when the aircraft was inside clouds and for estimates of general parameters like mean cloud particle diameter.

2.2 AIRTOSS

AIRTOSS, as shown in Fig. 2 (b), has a length of 2.85 m and a diameter of 24 cm; the maximum payload is 40 kg. It can be released from and retracted to the aircraft by a 4 km long towing cable. In the front part of AIRTOSS the Cloud Combination Probe (CCP, see e.g., Wendisch and Brenguier, 2013; Klingebiel et al., 2015) is installed. The CCP consists of the Cloud Droplet Probe (CDP) and the Cloud Imaging Probe instrument (CIP grey scale – denoted as CIPgs in the following). The CDP measurement principle is similar to the FSSP–100 and detects particles in the size diameter range between 2 µm and 50 µm by measuring the forward–scattered light of a laser beam which hits individual particles. The CIPgs records two–dimensional (2D) shadow images of the particles and covers a size range between 15 µm and 960 µm with an optical resolution of 15 µm. The performance of these microphysical cloud probes in cirrus clouds was characterized by McFarquhar et al. (2007). The center part of AIRTOSS contains a battery for power supply, which is sufficient to assure electrical power for measurements of about two hours. The radiation setup is mounted in the backward part of AIRTOSS. It consists of two spectrometer pairs and two optical inlets, one upward and one downward looking, measuring the downward and upward spectral irradiance F. Additional sensors for static air temperature and relative humidity, latitude, longitude and position angles pitch, roll and heading of AIRTOSS are installed.

The housing of the towed platform consists of an aerodynamic canister to avoid irregular movements and to enable quiet flying, which is crucial for reliable radiation measurements (Frey et al., 2009).

3 Optical layer properties

Four optical inlets, two for upward and two for downward irradiance measurements were mounted on the Learjet 35A and AIRTOSS. This setup enabled to simultaneously measure the irradiance in two different altitudes (e.g., above and below cloud) as required to calculate cloud layer properties (see Fig. 3). By measuring the upward and downward irradiances at the top and base of a cloud layer the optical properties are derived as follows. The reflectivity R is given by:

$$R = \frac{F^{\uparrow}{}_{\text{top}} - F^{\uparrow}{}_{\text{base}}}{F^{\downarrow}{}_{\text{top}}}. \tag{1}$$

R quantifies the relative portion of incoming solar radiation that is reflected by the cloud layer. The transmissivity T of a cloud layer is defined by:

$$T = \frac{F^{\downarrow}{}_{\text{base}}}{F^{\downarrow}{}_{\text{top}}}. \tag{2}$$

It describes the part of the incoming irradiance transmitted through the cloud. The relative portion of irradiance absorbed inside the cloud layer is defined by the absorptivity:

$$A = \frac{(F^{\downarrow}{}_{\text{top}} - F^{\uparrow}{}_{\text{top}}) - (F^{\downarrow}{}_{\text{base}} - F^{\uparrow}{}_{\text{base}})}{F^{\downarrow}{}_{\text{top}}}. \tag{3}$$

Equation 3 implicitly assumes that there are no horizontal components of radiative flux divergence, only vertical flux divergences are considered to derive absorptivity. From these definitions it follows:

$$R+T+A=\frac{F^{\uparrow}{}_{\text{top}}-F^{\uparrow}{}_{\text{base}}+F^{\downarrow}{}_{\text{base}}+F^{\downarrow}{}_{\text{top}}-F^{\uparrow}{}_{\text{top}}-F^{\downarrow}{}_{\text{base}}+F^{\uparrow}{}_{\text{base}}}{F^{\downarrow}{}_{\text{top}}}=1. \qquad (4)$$

The cloud top albedo R_{top} is given by:

$$R_{\text{top}}=\frac{F^{\uparrow}{}_{\text{top}}}{F^{\downarrow}{}_{\text{top}}}. \qquad (5)$$

R_{top} describes the cloud reflection property of the cloud layers and the underlying surface. For investigating the effect of a cirrus layer on the atmospheric radiative energy budget the radiative forcing (RF_{toa}) at the top of atmosphere (toa) is used, defined by:

$$RF_{\text{toa}}=(F^{\downarrow}{}_{\text{toa}}-F^{\uparrow}{}_{\text{toa}})_{\text{cloud}}-(F^{\downarrow}{}_{\text{toa}}-F^{\uparrow}{}_{\text{toa}})_{\text{clear sky}}. \qquad (6)$$

The subscripts "cloud" and "clear sky" indicate measurements or simulations in cloudy conditions and in a clear sky atmosphere. A positive RF_{toa} indicates a warming effect of the cloud on the underlying atmosphere and surface, whereas a negative RF_{toa} indicates a cooling effect.

4 Observations

Measurements were performed during two observational campaigns in spring (6 – 8 May) and late summer (29 August – 5 September) in 2013. The research flights were based at the military airports in Hohn and Jagel, North Germany, and were carried out in restricted flight areas above the North and Baltic Sea. The measurement areas represent boxes with the size of 50 x 80 km^2, and 35 x 80 km^2, respectively. Stepwise horizontal flight patterns were flown to collect radiative and microphysical data at different altitudes (6 – 11.5 km). The transport of tropospheric air masses into the stratosphere was reported by Mueller et al. (2015). In total, twelve measurement flights were carried out during both campaigns; four of them were analyzed in detail.

Measurements are presented of one exemplary flight which took place west of the German island of Helgoland above the North Sea (54.98° – 54.43°N, 6.59° – 7.57°E); it was performed on 30 August 2013 (08:33 – 09:48 UTC). Northern Germany was under the influence of an occluded front with associated cirrus and the center of the low south of Norway (see Fig. 4).

Fig. 4 (a) shows the corresponding composite satellite image of METEOSAT–10. In the image the high cirrus clouds are indicated by white color. Low clouds are labelled by yellow color and were present over a large area, including parts of the measurement area. The flight track of the Learjet 35A is shown in Fig. 4 (b).

4.1 Microphysical measurements

Fig. 5 shows the vertical profiles of (a) static air temperature (in °C), (b) relative humidity (in %) with respect to ice, measured by instruments on the aircraft, (c) number concentration (in cm^{-3}), and (d) mean diameter (in µm), measured by the CIPgs on AIRTOSS. The bars quantify the measurement errors, resulting from instrument uncertainties (a, b), counting statistics (c), and determination of the depth of field (d). Considering the measured ice particle number concentration the cirrus was identified in altitudes between 6.7 km and 8.5 km and between 9.0 km and 9.2 km, with a temperature range of $-21\,^{\circ}\mathrm{C}$ to $-39\,^{\circ}\mathrm{C}$.

Fig. 5 (c) and (d) show the particle number concentration and mean diameter as a function of altitude. Each data point is a mean value for a 200 m height interval. The cirrus layer between 6.7 and 8.5 km shows values for the number concentration of $1.2 \text{ x } 10^{-4}\,\mathrm{cm}^{-3}$ to $2.1 \text{ x } 10^{-3}\,\mathrm{cm}^{-3}$ and for the mean diameter of 145.6 and 178.3 μm, representing an optically thin and vertically well mixed cirrus. The gaps of measured number concentration and mean diameter are due to measurements outside the observed cirrus. The second cirrus layer between 9.0 and 9.2 km altitude shows increased values for the number concentration of up to $7.9 \text{ x } 10^{-3}\,\mathrm{cm}^{-3}$ and lower values for the mean diameter of 33.5 to 87.4 μm. This results in an optically thicker cirrus in comparison to a 200 m thick part of the cirrus layer between 6.7 and 8.5 km altitude.

4.2 Radiation data

4.2.1 Spectral irradiances

In Fig. 6 (a) the time series of downward and upward irradiance measured by AIRTOSS at a wavelength of 550 nm is illustrated for the entire flight: gray for downward and light blue for upward irradiance. The altitude of the Learjet (dashed red line in Fig. 6 (b)) and AIRTOSS (solid red line) show the stepwise climbing flight pattern and the different altitudes of the level legs as well as the vertical distance of about 200 m between both. The gray colored peaks in the time series of the irradiance (Fig. 6 (a)) are due to flight manoeuver and have to be excluded from further analysis. The measured pitch and roll angles of the AIRTOSS were used to sort out the data assuming a threshold of 5°. Resulting are the thickened line periods marking the measuring points at straight flight legs. The almost constant values of the downward irradiance ($1.09 - 1.20\,\mathrm{W\,m^{-2}\,nm^{-1}}$) are a result of the thin cirrus layer above the sensor. The upward irradiance is influenced by the surface albedo and changing conditions due to underlying clouds; they show values between 0.56 and $0.81\,\mathrm{W\,m^{-2}\,nm^{-1}}$ at 550 nm.

As the AIRTOSS is dragged behind the aircraft time allocation of the radiation measurements of the towed platform has to be adjusted to that measured simultaneously on the Learjet 35A to guarantee clear vertical collocation of the measurements. The temporal shift between the aircraft and AIRTOSS was calculated by using the cable length (914 m), aircraft velocity ($150 - 170\,\mathrm{ms^{-1}}$) and altitude difference of both platforms, as a function of the true air speed. The resulting altitude and time difference varies between 160 m and 210 m, corresponding to 4.8 seconds to 6 seconds.

Mean values of measured spectra of upward and downward irradiance from both platforms are shown in Fig. 7 from the time interval, indicated by the dashed lines in Fig. 6. The investigated cirrus layer is located between 9 and 9.2 km altitude and can be seen in Fig.5 (c) and (d), indicated by the upper gray colored layer. This measurement example was chosen due to the higher optical thickness, as reported in Section 4.1, and because of the low vertical extent, which enables to measure above and below this cirrus layer.

The vertical difference between the two measurement platforms is 195 m in the specific example discussed here. The downward irradiance $F^{\downarrow}{}_{\mathrm{top}}$ at the top of the cloud layer was simulated (Mayer and Kylling, 2005). The black solid lines show the irradiance, measured in the flight altitude of the Learjet above the cloud layer (subscript top), the black dotted lines represent the irradiance measured from the AIRTOSS at the base of the investigated part of the cirrus layer (subscript base).

As expected, the downward irradiance below the cirrus ($F^{\downarrow}{}_{\mathrm{base}}$) is lower than that measured above the cloud ($F^{\downarrow}{}_{\mathrm{top}}$). This shows that the attenuation of the solar radiation (reflection and absorption by cirrus particles) by the observed cirrus can actually be quantified by observational means. The upward irradiances ($F^{\uparrow}{}_{\mathrm{top}}$ and $F^{\uparrow}{}_{\mathrm{base}}$) are relatively high. This is due to low clouds, which were present below the cirrus in the measurement area during the selected measurement period. In case of an atmosphere without clouds in between the cirrus and the ocean surface (dashed line), lower upward irradiance data have been measured. Due to the high altitude, about 9.2 km, no water vapor absorption bands are revealed in the near infrared spectra as shown by the almost unaffected downward irradiance in both levels. Therefore, all absorption of solar radiation, measured in the downward irradiance below the cirrus, originates from the cirrus itself.

The upward radiation depends on the albedo of the Earth's surface and underlying clouds, as can be seen in enhanced values of upward irradiance. The absorption bands of liquid water at wavelengths of 1140 nm or 1400 nm are obvious in the spectra. Furthermore, the irradiances $F^{\uparrow}$ at both altitudes are similar. In comparison to the bright surface the difference due to the cirrus is not significant.

4.2.2 Spectra of reflectivity, absorptivity, transmissivity

By measuring the spectral and collocated upward and downward irradiances at two altitudes the cloud optical layer properties of the cirrus layer are derived according the Eq. (1) – (3) are derived. Fig. 7 (b) shows the spectral transmissivity (red, see Eq. 2), reflectivity (black, see Eq. 1), absorptivity (green, see Eq. 3), and cloud top albedo (gray, see Eq. 5) in the visible and near infrared wavelength range according to the example in Fig. 7 (a). The error bars result from the Gaussian error propagation due to uncertainties of calibration, of deviations from the ideal cosine angular sensor response correction, dark current, and signal to noise ratio. The resulting percentage errors range between 5 % and 6 % with higher values for the near infrared wavelength range.

As cirrus clouds are optically thin, the transmissivity dominates over the entire spectral range with high values between 88 % and almost 100 %. The reflectivity in Fig. 7 (b) shows very low values of not more than 3 %. This is due to the optically and vertically thin cirrus layer and a brighter water cloud underneath. The effect of the low cloud is indicated by the cloud top albedo showing high values of about 40 % to 60 % in the depicted wavelength range.

The transmissivity shows a slightly negative spectral slope, absorptivity a positive trend, and the reflectivity shows no spectral trend. As the imaginary part of the refractive index is associated with the absorption coefficient, which increases with increasing wavelength, the measured absorptivity shows a spectral trend with a positive slope and values up to 12 % in the near infrared range, pointing out the importance of cirrus clouds in this wavelength range.

A time series of the cloud optical layer properties (at 1640 nm) is given in Fig. 8, with (a) transmissivity, (b) absorptivity, and (c) reflectivity, for the cirrus layer between 9.0 and 9.2 km altitude and a horizontal distance of 10.4 km. The cloud top albedo from below the aircraft (gray triangles), representing the cirrus and low–level cloud is plotted in (d).

The right panels (e)–(h) show the histograms for the respective cirrus properties in the left representing the variability during this flight part. As T, A, and R are cloud layer properties, the varying values are due to changing optical and microphysical properties of the cirrus. The layer properties of this thin cirrus show small variations, thus indicating small spatial heterogeneity of the cirrus optical layer properties. The transmissivity reveals the smallest variation between 0.890 and 0.925 (4 %). Absorptivity and reflectivity range between 0.078 and 0.098, and 0.001 – 0.008, resulting in a percentage difference of 21 % and 87 %, respectively, but still within the error bars.

The larger variability of R_{top} is explained by the changing reflectivity properties of the surface on the cloud top albedo. As the cirrus layer is optically thin, R_{top} from above the cirrus is strongly affected by the surface albedo and bright underlying water clouds resulting in R_{top} variations of about 11 % and significant differences in the absolute values.

5 Radiative transfer simulation

5.1 Model introduction

To compare the measurements with simulations and for a measurement – based quantification of the impact of different parameters, such as cloud particle shape and size on cirrus cloud optical layer properties, sensitivity studies with the one–dimensional (1D) radiative transfer model libRadtran (Mayer and Kylling, 2005) including the DISORT (DIScrete ORdinate Radiative Transfer) code by Stamnes et al. (2000) are performed. The observed cirrus layer is represented by varying cloud properties and the corresponding upward and downward irradiance at the top and the base of the cirrus are calculated to obtain the optical layer properties reflectivity, absorptivity, and transmissivity (according to Eq. (1) – (3)), and the cloud top albedo and radiative forcing (Eq. (5) – (6)).

The needed volumetric extinction coefficient $\langle b_{\text{ext},\lambda} \rangle$, single–scattering albedo $\langle \omega_\lambda \rangle$, and phase function $\langle p_\lambda \rangle$ are derived by combining calculated tables of single scattering properties by Yang et al. (2005) with a specific in situ measured number size distribution $\mathrm{d}N\,/\,\mathrm{d}D$ (in cm^{-3}) from the CCP installed on AIRTOSS. The single scattering properties for individual particles (extinction coefficient $C_{\text{ext},\lambda}$, scattering coefficient $C_{\text{sca},\lambda}$, single–scattering albedo ω_λ, and phase function p_λ) with different particle radii are weighted with the number size distribution. The resulting spectral volumetric properties are used as input parameters for the radiative transfer simulations. The spectral volumetric extinction coefficient $\langle \mathrm{b}_{\text{ext},\lambda}\rangle$ in units of km^{-1} was obtained by (see Wendisch et al., 2005):

$$\langle b_{\text{ext},\lambda}\rangle = \int C_{\text{ext},\lambda} \cdot \frac{dN}{dD} \cdot dD. \tag{7}$$

The boundaries of integration are defined by the size diameter range of the CCP. A similar algorithm was used to derive the spectral volumetric single–scattering albedo $\langle \omega_\lambda \rangle$ by calculating:

$$\langle \omega_\lambda \rangle = \frac{\int \omega_\lambda \cdot C_{\text{ext},\lambda} \cdot \frac{dN}{dD} \cdot dD}{\langle b_{\text{ext},\lambda}\rangle}. \tag{8}$$

Furthermore, the volumetric phase function $\langle p_\lambda \rangle$ is obtained by:

$$\langle p_\lambda \rangle = \frac{\int p \cdot C_{\text{sca},\lambda} \cdot \frac{dN}{dD} \cdot dD}{\int C_{\text{sca},\lambda} \cdot \frac{dN}{dD} \cdot dD}. \tag{9}$$

5.2 Simulated spectra for individual cirrus layer

To compare, in a first step, the measured cloud optical layer properties R, T, A, and cloud top albedo R_{top} with the simulated quantities, Fig. 10 (a) – (e) shows simulations of a cirrus layer between 9.0 and 9.2 km altitude with different optical thicknesses. The input for the simulations includes a measured number size distribution, shown in Fig. 9, which was measured during the AIRTOSS campaign and represents a typical cirrus. The ice crystal shape is assumed do be constant, further assuming a mixture of particle shapes according to Baum et al. (2005).

The cirrus optical thickness varies between 0.11 and 0.55. As expected, an increasing optical thickness leads to a decreased transmissivity T and increased reflectivity R, absorptivity A, and cloud top albedo R_{top}. The spectral trend shows pronounced effects for T and A in the near infrared wavelength range excluding the ranges of the water vapor absorption bands resulting in percentage differences of 10 % and a factor of 5, respectively, between the optically thinnest and thickest cloud layer. The absorptivity varies in the range of the ice particle absorption and causes a difference by up to a factor of 5, whereas the cloud top albedo shows a similar difference of a factor of 5 in the wavelength range of water vapor absorption. According to the changes in the layer properties, the radiative forcing varies most between those cases while the absolute differences are small, varying between -0.006 and -0.033 $\mathrm{W\,m^{-2}\,nm^{-1}}$ (at 550 nm).

Comparing the measured (diamonds) and simulated (lines) spectral cloud optical layer properties, it can be seen, that there are visible discrepancies due to different possible input parameters such as optical thickness, ice crystal shape, and properties of the underlying surface.

As a cirrus cloud of 200 m vertical extent is not a typical one, for further sensitivity studies a cirrus between 6.7 and 8.5 km altitude is assumed, according to the measurement case of 30 August 2013 (see Fig. 5). The implemented number size distribution (Fig. 9) and the assumption of a mixture of shapes, described by Baum et al. (2005), results in an cirrus optical thickness of 1, representing a typical cirrus cloud.

To investigate the effect of different ice crystal shapes (see Fig. 11), a fixed number size distribution is combined with different shape assumptions: Solid Column, Column – 8 Elements, Plate, Plate 10 – Elements, Solid Bullet Rosette, Droxtal, and a mixture of 30 % Plates (10 Elements), 30 % Hollow Bullet Rosettes, 20 % Plates, and 20 % Hollow Columns, similar to the mixture according to Baum et al. (2005). The multi–component ice crystals, such as Column – 8 Elements, are aggregates consisting of their respective number of crystals. The different crystal shapes are introduced by Yang et al. (2013). The ice crystal roughness is set to smooth, see Baum et al. (2010).

Two approaches are investigated: (I) the number size distribution is constant (NSD, left panels), (II) the ice water content is constant (IWC, right panels). As the number size distribution is derived from in situ measurements, assuming a constant IWC is a more physical approach.

Fig. 11 shows the simulated (lines) spectral optical layer properties transmissivity T (a,e), reflectivity R (b,f), and absorptivity A (c,g) for those crystal shapes. Additionally, the simulated radiative forcing RF_{toa} (see Eq. 6) in (e,h) are represented. As reference case the shape Droxtal (red line) is used approximating spherical particles. Table 1 shows the resulting optical thicknesses assuming different shapes for the two approaches.

The results for approach I show, that varying ice crystal shape causes differences that are spectrally dependent, especially for absorptivity in the near infrared wavelength range between 1450 and 1800 nm, and 1900 and 2200 nm, where the imaginary part of the refractive index of ice reveals a maximum. This corresponds to an increased absorption coefficient and, therefore, a pronounced shape effect in this wavelength range. A similar spectral trend of the shape effect shows the transmissivity.

The percentage difference of transmissivity between the varying shapes and the reference case (Droxtals) ranges between 5 % and 50 %. The lowest differences show Solid Columns and Plates, whereas the mixture according to Baum et al. (2005) and Plates (10 Elements) show highest values. The shape variability is more pronounced for reflectivity and absorptivity with differences of up to 80 % and a factor of 2 for Plates (10 Elements), respectively.

In relation to the highest values of reflectivity the corresponding radiative forcing for Solid Columns and Droxtals are strongest with -0.20 and -0.18 $\mathrm{W\,m^{-2}\,nm^{-1}}$ (at 550 nm) and for Plates (10 Elements) and the mixture according to Baum et al. (2005) lowest with -0.05 and -0.06 $\mathrm{W\,m^{-2}\,nm^{-1}}$ (550 nm), respectively, resulting in pronounced cooling effects for Droxtals and Solid Columns. This leads to a difference in the radiative forcing of a factor of up to 4 assuming different shapes.

Assuming a constant IWC of 0.395 $\mathrm{g\,m^{-3}}$ (approach II) for varying ice crystal shapes means keeping the total volume of the cirrus cloud particles constant. This leads to the largest variabilities between Droxtals, approximating spheres, and crystal shapes with a large surface area, such as aggregates of shapes or rosettes. For transmissivity and absorptivity the resulting differences are no more than 60 %. The largest differences (factor of 4) are obtained for the reflectivity as well as for radiative forcing by a factor of 6, due to the link between the total surface area of a cloud and its capability of reflection. In comparison with approach I the second scenario II shows significantly larger variabilities assuming different shapes for the cloud optical layer properties and radiative forcing.

5.3 Cirrus and underlying low–level cloud

Chang and Li (2005) reported an annual and global occurrence of high clouds of 52 – 61 % (ocean – land), from which 27 % to 29 % represent cases with low clouds underneath the cirrus. During the flights very often low clouds were observed, that is why the related effect of a low–level water cloud was investigated. Fig. 12 shows two cirrus cases, one with (black line) and one without (red line) a low–level water cloud. The cirrus is the same case as in Fig. 11, Approach I, assuming the mixture of shapes according to Baum et al. (2005). For the second case a water cloud (τ = 20) was added between 1 km and 1.25 km altitude. The measurement example is the same as shown in Fig. 7.

Adding a low–level cloud in the simulation leads to a higher transmissivity (up to 6 %) and lower reflectivity (up to 90 %) of the cirrus layer except in the wavelength ranges of the water vapor absorption bands. As the cloud top albedo is no cirrus layer property it shows the largest difference for the low–level cloud case, but a good agreement with the measurement case in the shortwave–infrared wavelength range.

For characterizing the effect of a low water cloud on the radiative forcing of the cirrus and the atmosphere's energy budget, a modified radiative forcing RF'_{Ci} is introduced:

$$RF'_{\text{Ci}} = RF_{\text{Ci+low cloud}} - RF_{\text{low cloud}} \tag{10}$$

$$RF'_{\text{Ci}} = F^{\uparrow}_{\text{low cloud}} - F^{\uparrow}_{\text{Ci+low cloud}}.$$

The resulting RF'_{Ci} is the difference between the case of a cirrus with underlying low water cloud and the case with the low cloud only (as Keil and Haywood (2003) applied for aerosol layers) at top of atmosphere.

RF'_{Ci} is shown in Fig. 12 (e) (black line) in contrast to the radiative forcing RF (see Eq. 6) of the same but single–layer cirrus (red line). It is noticeable that there is a sign changing effect on RF' with negative values for the visible spectral range and a positive radiative forcing in the near infrared range. This leads to an overestimation of the cooling effect of the cirrus with a percentage difference of about 80 % in the visible wavelength range and up to a factor of 2 in the near infrared range caused by the low–level cloud.

The results obtained in this paper are valid for the respective cloud cases. To evaluate the low–level cloud effect on the cirrus the properties of the low water cloud, such as optical thickness and cloud top height, have to be investigated, too. Therefore, Fig. 13 (a) and (b) show values of integrated cirrus radiative forcings (wavelength range: 300–2300 nm) with varying water cloud optical thickness

(a) and cloud top height (b). The cirrus is located between 6.7 km and 8.5 km altitude and consists of the mixture of shapes according to Baum et al. (2005). The color code represents the changing cirrus optical thickness.

In Fig.13 (a) the low–level cloud is located between 1 km and 1.25 km with an increasing optical thickness from 5 to 60. In general, the cooling of the cirrus decreases with increasing optical thickness of the low cloud resulting in an increasing influence of the low cloud on the upper lying cirrus. This is due to the reflected radiation by the low cloud being available to interact with the cirrus layer again. With higher water cloud optical thickness a saturating effect can be seen resulting in differences of 72 % to 83 %. Additionally, with increasing cirrus optical thickness the absolute difference of RF increases from $10\,\mathrm{W\,m^{-2}}$ to $32\,\mathrm{W\,m^{-2}}$.

In Fig.13 (b) the low water cloud has a constant optical thickness of 20, and a vertical thickness of 250 m with an increasing cloud top height from 1.25 to 7.25 km. Similar to Fig.13 (a) the cooling of the cirrus decreases with increasing cloud top height of the low–level cloud. Here, the amount of the reflected radiation by the low cloud, available in the cirrus level, depends on the vertical extension of the atmosphere in between and its interaction with the transmitted (from cirrus) and reflected (from water cloud) radiation. The trend of RF is similar to (a) with increasing cloud top height with a resulting in lower differences of 20 % to 35 % and absolute values of not more than $8\,\mathrm{W\,m^{-2}}$.

It is noticeable that the cloud optical thickness of the low cloud in comparison to the cloud top height has a significant effect on the radiative forcing of the above lying cirrus.

6 Conclusions

Spectra of optical layer properties of cirrus have been derived from the first truly collocated airborne radiation measurements in the framework of the AIRTOSS (AIrcraft TOwed Sensor Shuttle) project. The radiation measurements are complemented by microphysical in–situ measurements and radiative transfer simulations, based on the microphysical data.

Two field campaigns have taken place above the North Sea and the Baltic Sea in spring and late summer 2013. Collocated measurements by an aircraft (Learjet 35A) and the towed platform AIRTOSS, released on a towing cable underneath the plane, are collected above, beneath and inside the cirrus. For radiation measurements the straight flight legs with minor changes of pitch and roll movements of the measurement platform are selected for detailed analysis.

Spectral upward and downward irradiances in the visible and near infrared wavelength range above and below the cirrus have been measured to derive the spectral transmissivity, absorptivity, reflectivity, and cloud top albedo of the observed cirrus layer. Irradiance spectra and a time series for a straight flight leg of 30 August 2013 are analyzed. The resulting layer properties at one wavelength in the near infrared (1640 nm) differ only slightly due to horizontal inhomogeneities and the influence of low–level clouds, but with an increased effect due to low clouds in the cloud top albedo with varying values of up to 11 %.

The impact of varying ice crystal shape and cloud particle size distribution is studied with a 1D radiative transfer model in combination with volumetric extinction coefficient, single–scattering albedo, and phase function calculated from measured in situ size distributions and tables of ice crystal single–scattering properties. The results show the highest sensitivity in cloud optical layer properties for varying ice crystal shapes for the absorptivity with up to a factor of 2 with respect to the reference case of nearly spherical shaped Droxtals. The respective cirrus radiative forcing differs by a factor of up to 4 with a stronger cooling effect for Droxtals. A similar effect is due to an additional low–level water cloud, as observed during the measurement flights, with a noticeable difference in the reflectivity of the above lying cirrus of up to a factor of 2 under multi–layer conditions. The radiative forcing of the cirrus layer may switch sign and shows positive values in the near infrared wavelength range with a resulting difference of up to a factor of 2. It was found that if a low–level cloud is not considered the solar cooling of the cirrus is strongly overestimated. The variation of the low–level cloud properties cloud top height and optical thickness influences the cirrus radiative forcing, too, resulting in differences of 35 and 83 %, respectively.

The application of measured in situ microphysical properties as input of radiative transfer simulations did not accurately reproduce the measured cirrus optical layer properties. This is partly due to a variety of possible shapes and mixtures of shapes, and influenced by a changing albedo. Further adjustment of the simulations can probably be used to optimize the agreement and derive more information on the particle properties. The effect of the low–level water cloud has to be further investigated by varying the property of the cirrus, such as shape, size, and height of the cloud base and top. As the interaction of the cirrus with terrestrial radiation is the important factor for affecting the Earth's energy budget, radiative transfer calculations in the terrestrial wavelength range have to be investigated.

Acknowledgements. This study was supported by the Deutsche Forschungsgemeinschaft through Project "WE 1900/19–1, BO 1829/7–1". Additional funding on a similar level for the aircraft certification of AIRTOSS and for conducting the campaign was provided by internal sources of the Particle Chemistry Department at the Max Planck Institute for Chemistry. We thank the pilots and crew of the Gesellschaft für Flugzieldarstellung (GFD) and enviscope GmbH for preparation and execution of the test and research flights, and the colleagues from Forschungszentrum Jülich and University of Warsaw for their support.

References

Baum, B. A., Yang, P., Heymsfield, A. J., Platnick, S., King, M. D., Hu, Y. X., and Bedka, S. T.: Bulk scattering properties for the remote sensing of ice clouds. Part II: Narrowband models, J. Appl. Meteor., 44, 1896–1911, 2005.

Baum, B. A., Yang, P., Hu, Y. X., and Feng, Q. A.: The impact of ice particle roughness on the scattering phase matrix RID B-7670-2011 RID B-4590-2011, J. Quant. Spectrosc. Radiat. Transfer, 111, 2534–2549, doi:10.1016/j.jqsrt.2010.07.008, 2010.

Bierwirth, E., Wendisch, M., Ehrlich, A., Heese, B., Tesche, M., Althausen, D., Schladitz, A., Müller, D., Otto, S., Trautmann, T., Dinter, T., von Hoyningen-Huene, W., and Kahn, R.: Spectral surface albedo over Morocco and its impact on the radiative forcing of Saharan dust, Tellus, 61B, 252–269, 2009.

Chang, F.–L., Li, Z.: A Near-Global Climatology of Single-Layer and Overlapped Clouds and Their Optical Properties Retrieved from Terra/MODIS Data Using a New Algorithm, J. of Climate, 18, 4752–4771, 2005.

Eichler, H., Ehrlich, A., Wendisch, M., Mioche, G., Gayet, J.-F., Wirth, M., Emde, C., and Minikin, A.: Influence of ice crystal shape on retrieval of cirrus optical thickness and effective radius: A case study, J. Geophys. Res., 114, D19203, doi:doi:10.1029/2009JD012215, 2009.

Field, P. R., Wood, R., Brown, P. R. A., Kaye, P. H., Hirst, E., Greenaway, R., and Smith, J. A.: Ice particle interarrival times measured with a fast FSSP, J. Atmos. Oceanic Technol., 20, 249–261, 2003.

Field, P. R., Heymsfield, A., and Bansemer, A.: Shattering and particle interarrival times measured by Optical Array Probes in ice clouds, J. Atmos. Oceanic Technol., 23, 1357–1370, 2006.

Francis, P., Hignett, P., and Macke, A.: The retrieval of cirrus cloud properties from aircraft multi-spectral reflectance measurements during EUCREX ’93, Quart. J. Roy. Meteor. Soc., 124, 1273–1291, 1998.

Frey, W., Eichler, H., de Reus, M., Maser, R., Wendisch, M., and Borrmann, S.: A new airborne tandem platform for collocated measurements of microphysical cloud and radiation properties, Atmos. Meas. Tech., 2, 147–158, 2009.

Gayet, J. F., Auriol, F., Minikin, A., Strom, J., Seifert, M., Krejci, R., Petzold, A., Febvre, G., and Schumann, U.: Quantitative measurement of the microphysical and optical properties of cirrus clouds with four different in situ probes: Evidence of small ice crystals, Geophys. Res. Lett., 29, 83-1 – 83-4, doi:10.1029/2001GL014 342, 2002.

Henrich, F., Siebert, H., Jäkel, E., Shaw, R. A., and Wendisch, M.: Collocated measurements of boundary-layer cloud microphysical and radiative properties and comparison with satellite retrievals, J. Geophys. Res., 115, D24 214, doi:10.1029/2010JD013930, 2010.

IPCC: Climate Change 2013: The Physical Science Basis, Cambridge University Press, Cambridge, United Kingdom and New York, NY, USA, 2013.

Keil, A. and Haywood, J. M.: Solar radiative forcing by biomass burning aerosol particles during SAFARI 2000: A case study based on measured aerosol and cloud properties, J. Geophys. Res., 108, 8467, doi:10.1029/2002JD002315, 2003.

Klingebiel, M., de Lozar, A., Molleker, S., Weigel, R., Roth, A., Schmidt, L., Meyer, J., A., E., Neuber, R., M., W., and Borrman, S.: Arctic low–level boundary layer clouds: in situ measurements and simulations of mono– and bimodal supercooled droplet size distributions at the top layer liquid phase cloud, Atm. Chem. Phys., 15, 617–631, 2015.

Korolev, A. V., Emery, E. F., Strapp, J. W., Cober, S. G., and Isaac, G. A.: Quantification of the Effects of Shattering on Airborne Ice Particle Measurements, J. Atmos. Ocean Technol., 30, 2527–2553, 2013.

Liou, K.-N.: Influence of cirrus clouds on weather and climate processes: A global perspective, Mon. Wea. Rev., 114, 1167–1199, 1986.

Lynch, K., Sassen, K., Starr, D., Stephens, G., Heymsfield, A., Liou, K.-N., Minnis, P., and Platt, C.: Cirrus, Oxford University Press, New York, 2002.

Mayer, B. and Kylling, A.: Technical note: The *libRadtran* software package for radiative transfer calculations - description and examples of use, Atmos. Chem. Phys., 5, 1855–1877, 2005.

McFarquhar, G. M., Um, J., Freer, M., Baumgardner, D., Kok, G. L., and Mace, G.: Importance of small ice crystals to cirrus properties: Observations from the Tropical Warm Pool International Cloud Experiment (TWP-ICE), Geophys. Res. Lett., 34, L13803, doi:10.1029/2007GL029865, 2007.

Müller, S., Hoor, P., Berkes, F., Bozem, H., Klingebiel, M., Reutter, P., Smit, H. G. J., Wendisch, M., Spichtinger, P., and Borrman, S.: In-situ detection of stratosphere-troposphere-exchange of cirrus particles in the mid-latitudes, Geophys. Res. Let., 42, doi:10.1002/2014GL062556, 2015.

Pilewskie, P. and Valero, F. P. J.: Radiative effects of the smoke clouds from the Kuwait oil fires, J. Geophys. Res., 97, 14 541–14 544, 1992.

Schlimme, I., Macke, A., and Reichardt, J.: The impact of ice crystal shapes, size distributions, and spatial structures of cirrus clouds on solar radiative fluxes, J. Atmos. Sci., 62, 2.274–2.283, 2005.

Stamnes, K., Tsay, S.-C., Wiscombe, W., and Laszlo, I.: DISORT, a General-Purpose Fortran Program for Discrete-Ordinate-Method Radiative Transfer in Scattering and Emitting Layered Media: Documentation of Methodology, Tech. rep., Dept. of Physics and Engineering Physics, Stevens Institute of Technology, Hoboken, NJ 07030, 2000.

Wendisch, M. and Brenguier, J.-L.: Airborne Measurements for Environmental Research – Methods and Instruments, Wiley–VCH Verlag GmbH & Co. KGaA, Weinheim, Germany, Weinheim, Germany, iSBN: 978-3-527-40996-9, 2013.

Wendisch, M., Müller, D., Schell, D., and Heintzenberg, J.: An airborne spectral albedometer with active horizontal stabilization, J. Atmos. Oceanic Technol., 18, 1856–1866, 2001.

Wendisch, M., Pilewskie, P., Pommier, J., Howard, S., Yang, P., Heymsfield, A. J., Schmitt, C. G., Baumgardner, D., and Mayer, B.: Impact of cirrus crystal shape on solar spectral irradiance: A case study for subtropical cirrus, J. Geophys. Res., 110, D03 202, doi:10.1029/2004JD005294, 2005.

Wendisch, M., Yang, P., and Pilewskie, P.: Effects of ice crystal habit on thermal infrared radiative properties and forcing of cirrus, J. Geophys. Res., 112, D03 202, doi:10.1029/2006JD007899, 2007.

Werner, F., Siebert, H., Pilewskie, P., Schmeissner, T., Shaw, R. A., and Wendisch, M.: New airborne retrieval approach for trade wind cumulus properties under overlying cirrus, J. Geophys. Res., 118, 3634–3649, doi:10.1002/jgrd.50334, http://dx.doi.org/10.1002/jgrd.50334, 2013.

Werner, F., Ditas, F., Siebert, H., Simmel, M., Wehner, B., Pilewskie, P., Schmeissner, T., Shaw, R. A., Hartmann, S., Wex, H., Roberts, G. C., and Wendisch, M.: Twomey effect observed from collocated microphysical and remote sensing measurements over shallow cumulus, J. Geophys. Res., 119, 1534–1545, doi:10.1002/2013JD020131, http://dx.doi.org/10.1002/2013JD020131, 2014.

Wylie, D., Menzel, W., Woolf, H., and Strabala, K.: Four years of global cirrus cloud statistics using HIRS, J. Climate, 7, 1972–1986, 1994.

Yang, P., Wei, H. L., Huang, H. L., Baum, B. A., Hu, Y. X., Kattawar, G. W., Mishchenko, M. I., and Fu, Q.: Scattering and absorption property database for nonspherical ice particles in the near- through far-infrared spectral region, Appl. Opt., 44, 5512–5523, 2005.

Yang, P., Bi, L., Baum, B. A., Liou, K. N., Kattawar, G. W., Mishchenko, M. I., and Cole, B.: Spectrall consistent scatterin, absorption, and polarization properties of atmospheric ice crystals at wavelengths from 0.2 to 100 μm, J. Atmos. Sci., 70, 330–347, 2013.

Zhang, Y., Macke, A., and Albers, F.: Effect of crystal size spectrum and crystal shape on stratiform cirrus radiative forcing, Atmos. Res., 52, 59–75, 1999.

Figure 1. Photo from the Learjet 35A with towed AIRcraft TOwed Sensor Shuttle. The picture was taken during a test flight from a second aircraft.

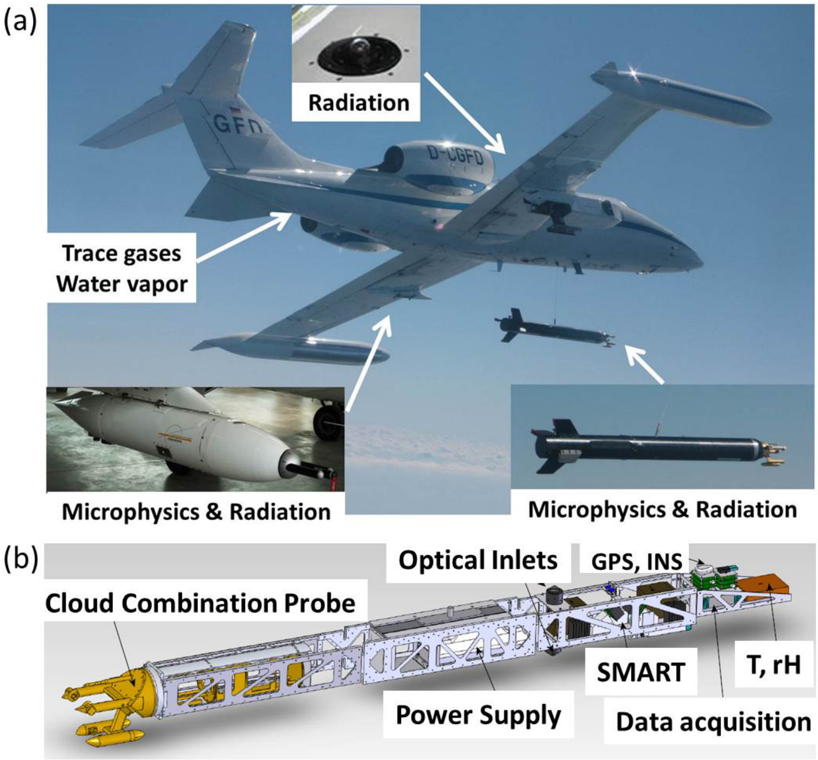

Figure 2. (a) Assembly of the research aircraft Learjet 35A, the towed AIRTOSS, and the wing pod containing instruments measuring radiation, microphysical parameter, water vapor, and trace gases. (b) Sketch of the AIRTOSS setup.

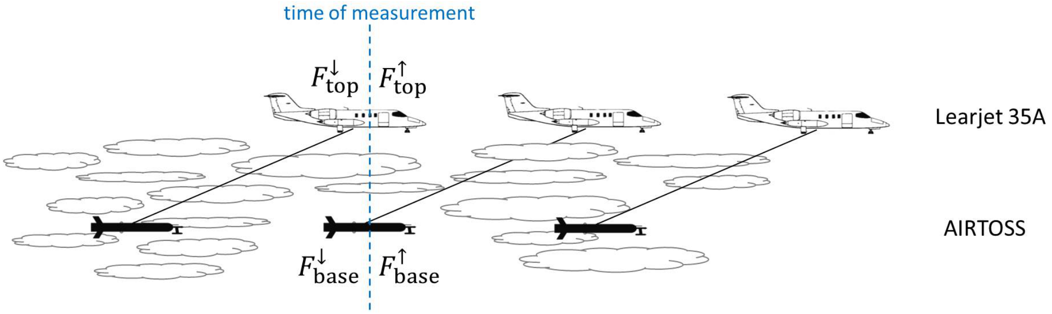

Figure 3. Schematic sketch of measurement setup to measure collocated upward ($F^{\uparrow}$) and downward ($F^{\downarrow}$) irradiance at two altitudes (base, top).

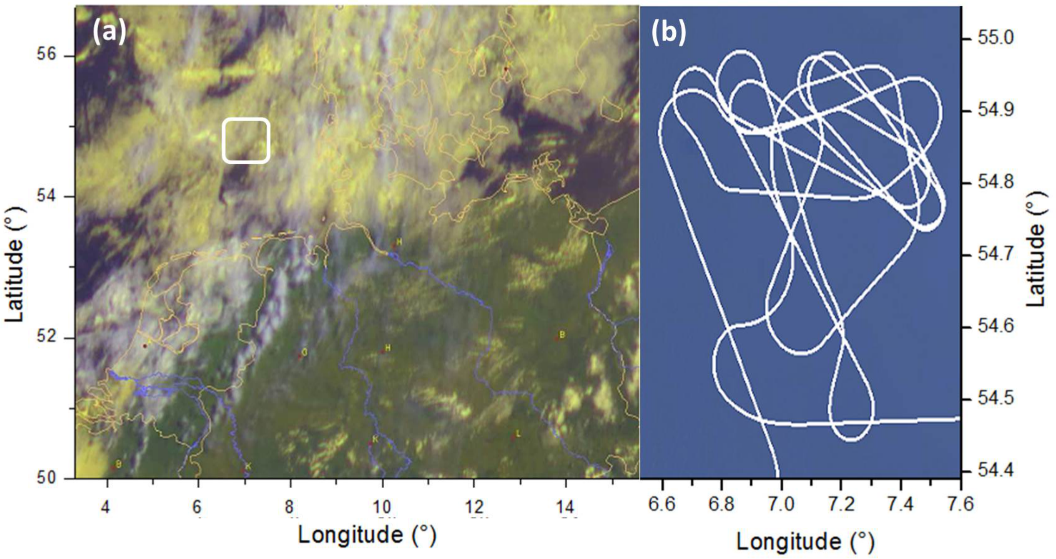

Figure 4. (a) Composite satellite image of the cloud situation on 30 August 2013 at 9:45 UTC showing cirrus (white) above yellow colored lower water clouds (Deutscher Wetterdienst / EUMETSAT). In (b) the flight track of the measuring flight in the restricted area (white box in (a)) above the North Sea near the island of Helgoland, North Germany, is shown.

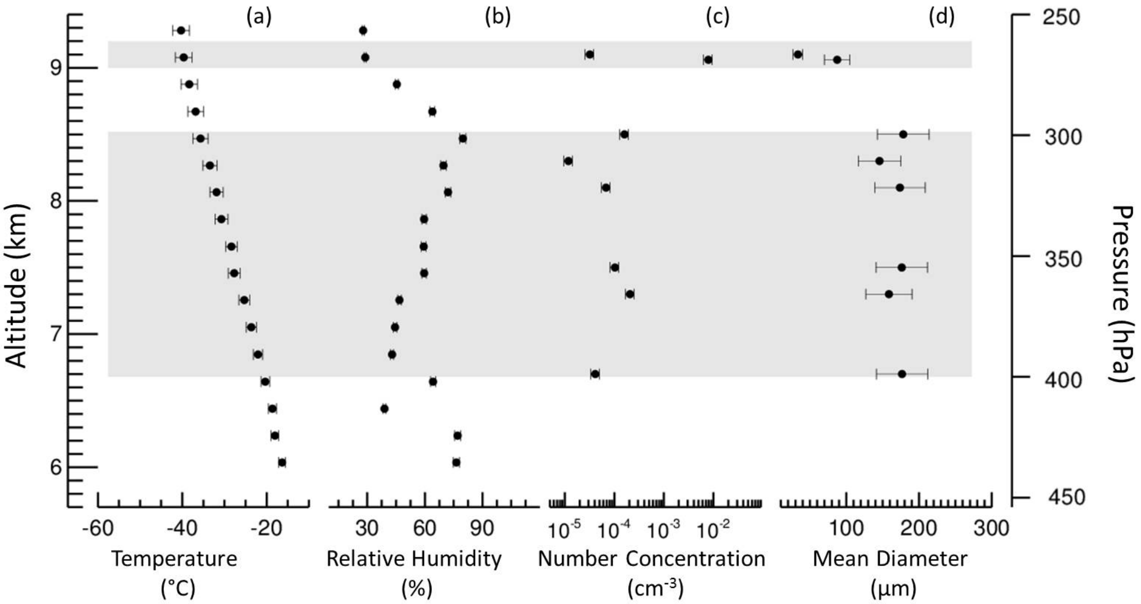

Figure 5. Vertical profiles of (a) temperature, (b) relative humidity, measured on the Learjet 35A, (c) number concentration, and (d) mean diameter, derived by CIPg on AIRTOSS, from the flight of 30 August 2013. The bars show the corresponding measurement uncertainties. The gray area indicates the vertical extent of the cirrus layer.

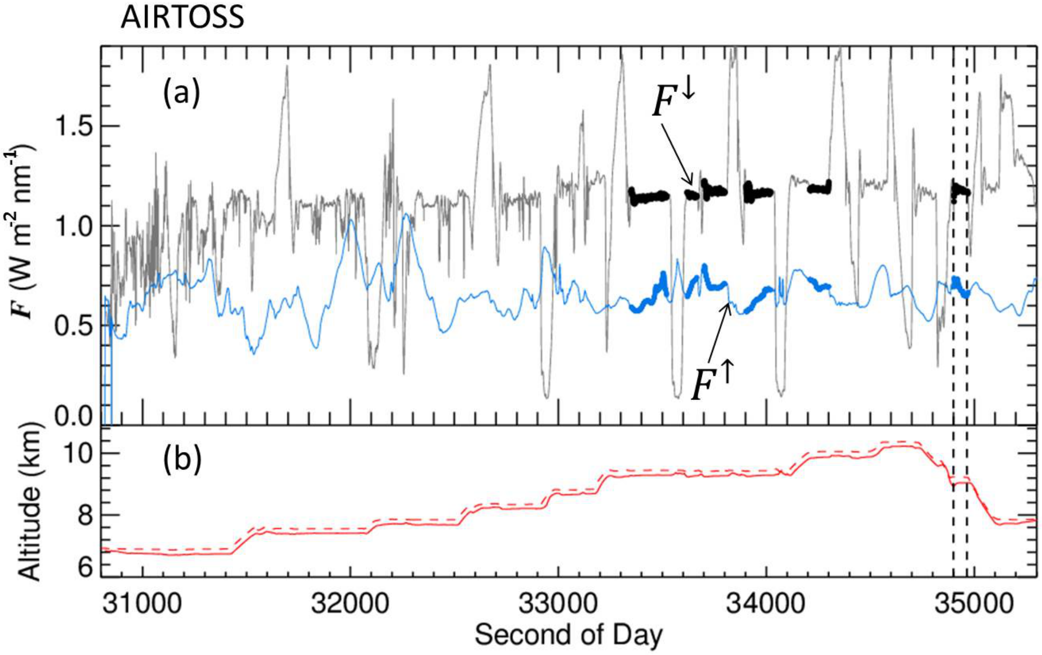

Figure 6. (a) Time series of downward (gray) and upward (light blue) irradiance F (W m^{-2} nm^{-1}) measured on AIRTOSS at one wavelength (550 nm) from the flight of 30 August 2013. The thickened line periods mark the measuring points at straight flight legs. The red lines in (b) show the altitude of AIRTOSS (solid) and Learjet (dashed). The vertical dashed line marks the measurement example in Fig. 7.

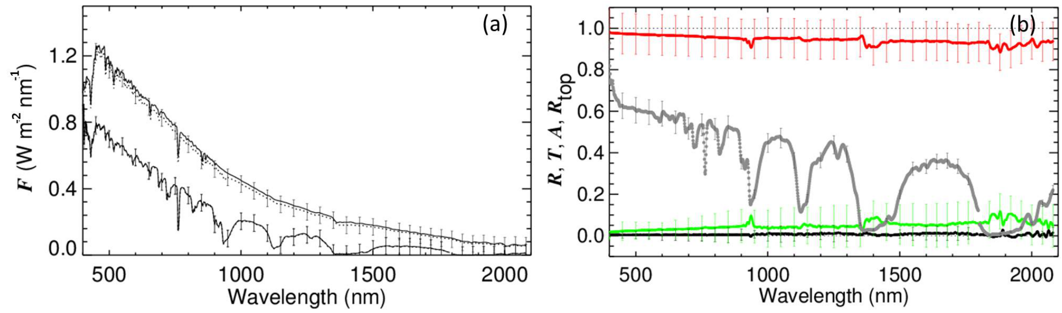

Figure 7. (a) shows measured spectral downward and upward irradiance F from the aircraft above the cloud layer (solid lines) and AIRTOSS below the cloud layer (dotted lines) at the time, indicated by the vertical dashed line in Fig 6. $F^{\downarrow}{}_{\text{top}}$ is simulated. (b) shows spectral reflectivity (black), transmissivity (red), absorptivity (green), and cloud top albedo (gray) according to irradiance in (a). The vertical bars indicate the systematic errors due to measurement uncertainties.

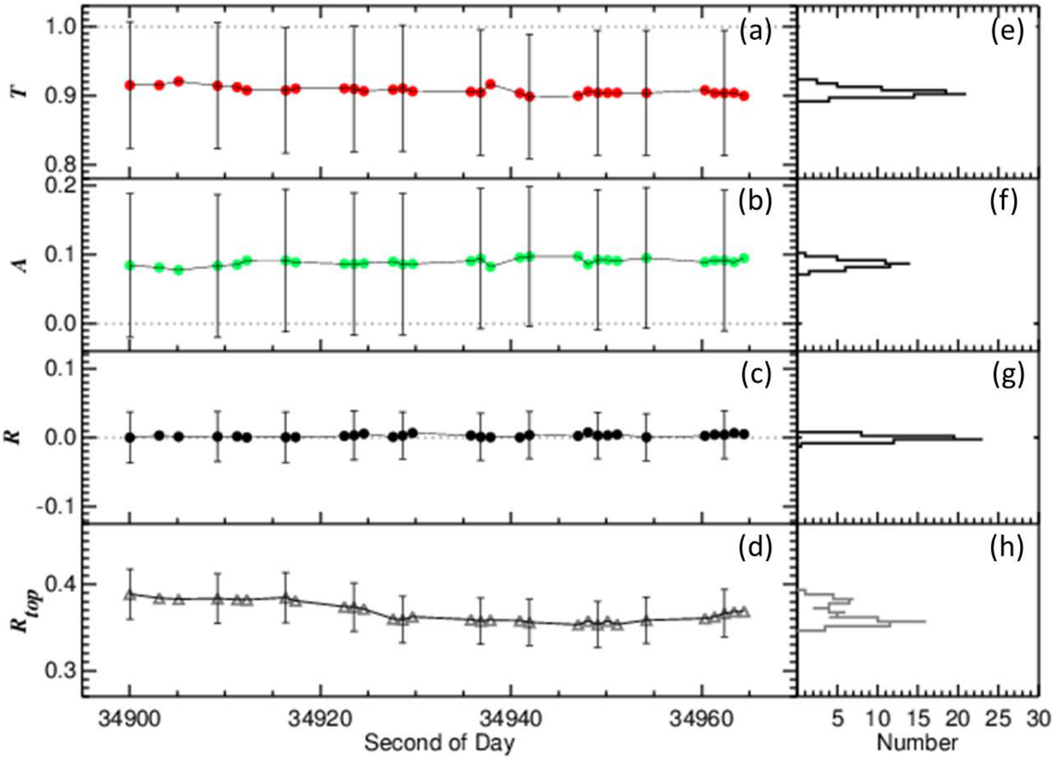

Figure 8. Shown are time series of (a) transmissivity, (b) absorptivity, and (c) reflectivity (at 1640 nm) for the cirrus layer between 9.0 and 9.2 km altitude on 30 August 2013. The associated cloud top albedo is plotted in (d). The vertical bars represent the errors due to measurement uncertainties. (e) – (h) show the histograms, respectively.

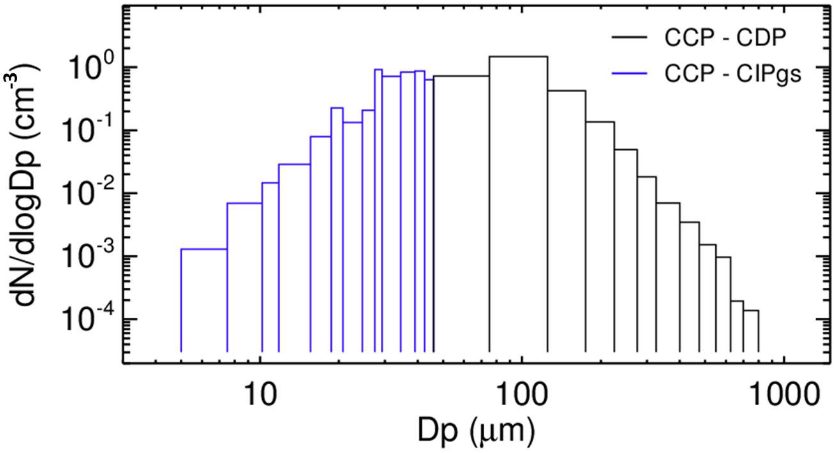

Figure 9. Number size distribution of a cirrus cloud, measured during the AIRTOSS campaign by the Cloud Combination Probe at the AIRcraft TOwed Sensor Shuttle.

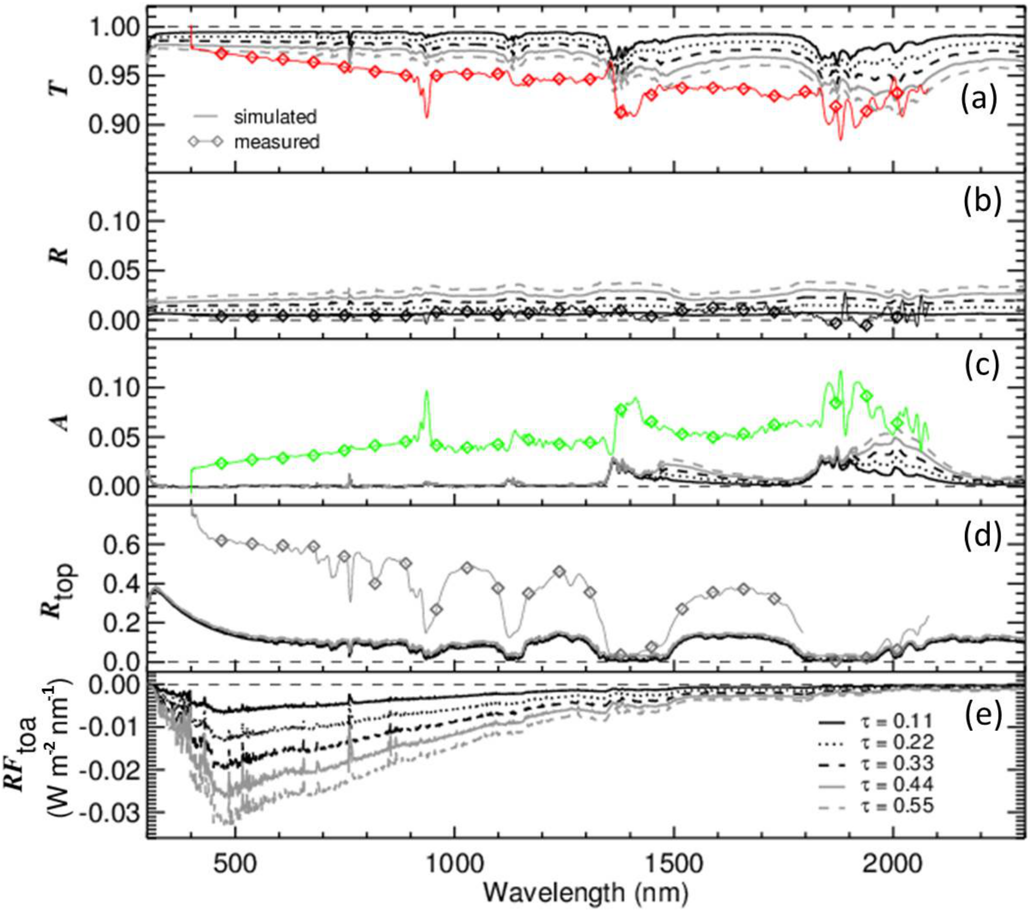

Figure 10. The lines show simulated, spectral (a) transmissivity, (b) reflectivity, and (c) absorptivity of a cirrus layer between 9 km and 9.2 km altitude. (e) are the radiative forcings at TOA, respectively. The simulations are based on a measured number size distribution assuming the mixture of shapes according Baum et al. (2005). Inserted is the measurement case (diamonds) from Fig.7.

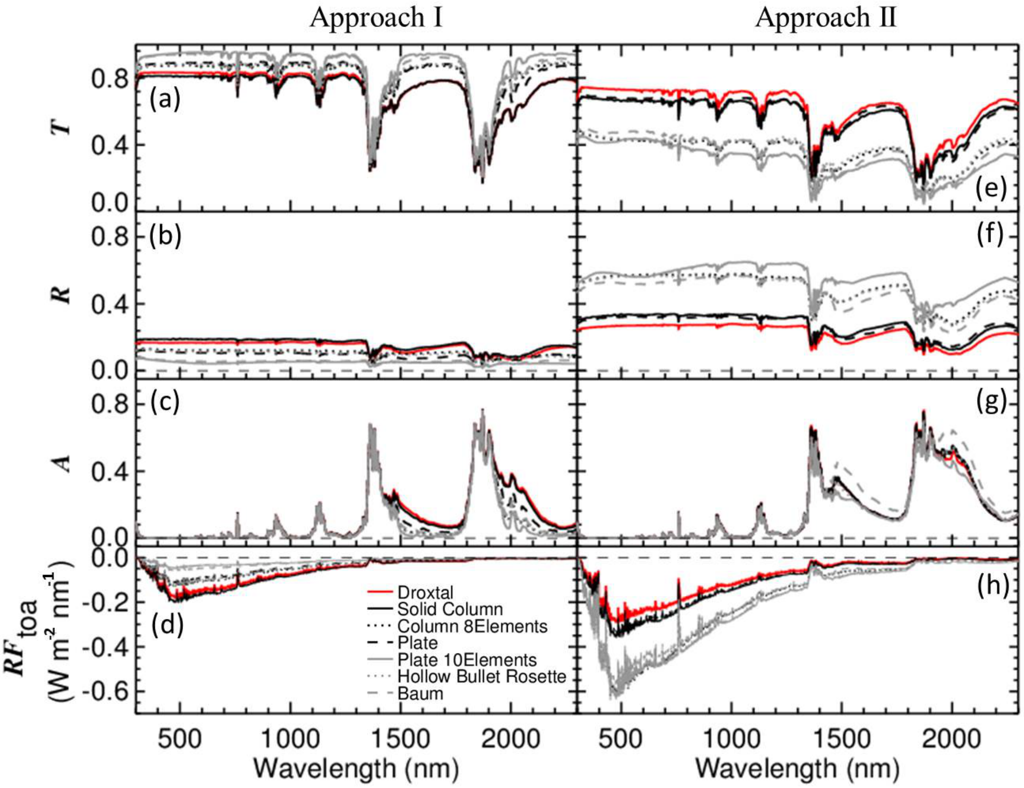

Figure 11. Shown are spectral (a,e) transmissivity, (b,f) reflectivity, and (c,g) absorptivity of a cirrus layer between 6.7 and 8.5 km altitude. (e,h) are the radiative forcings at TOA, respectively. The simulations are based on a measured number size distribution assuming different ice particle shapes. The two panels indicate two conditions: constant number size distribution (Approach I) and constant ice water content (Approach II).

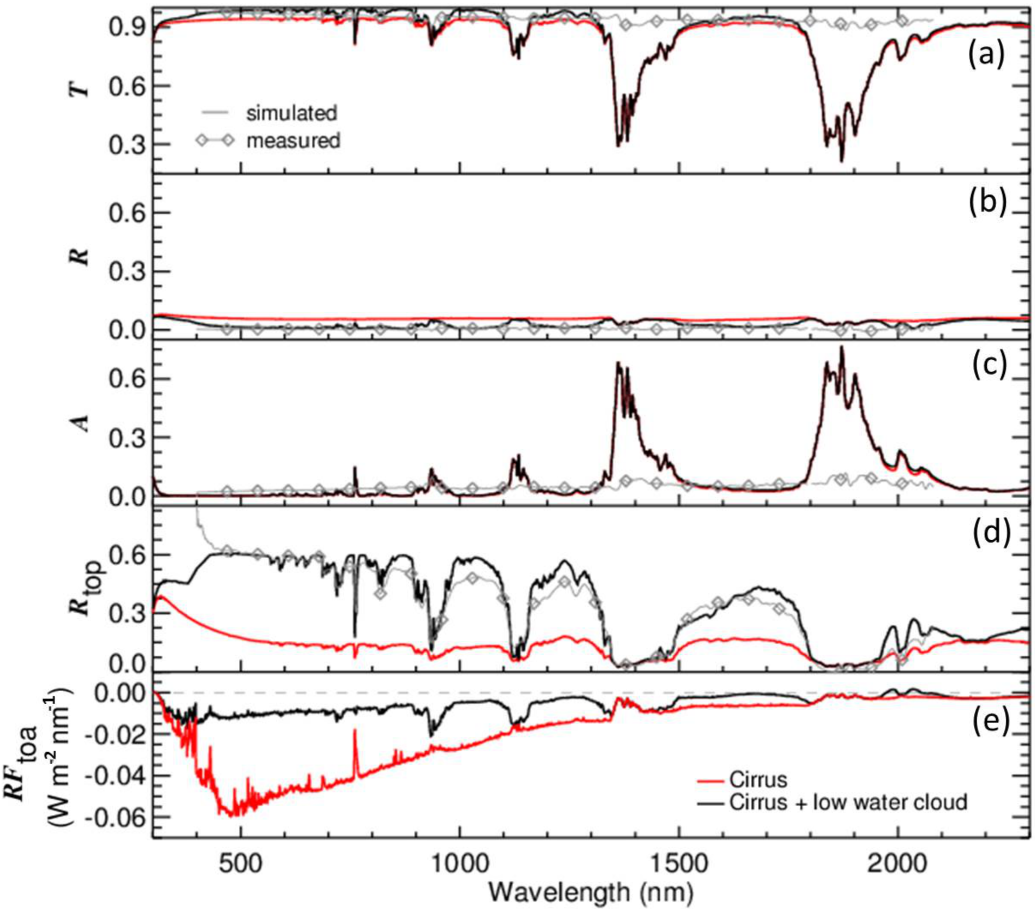

Figure 12. Same as Fig.10 assuming the mixture according to Baum et al. (2005) between 6.7 and 8.5 km altitude ($\tau_{\text{Cirrus}} = 1$). An additional low water cloud with $\tau = 20$ is included between 1.0 and 1.25 km altitude. Inserted is the measurement case (gray diamonds).

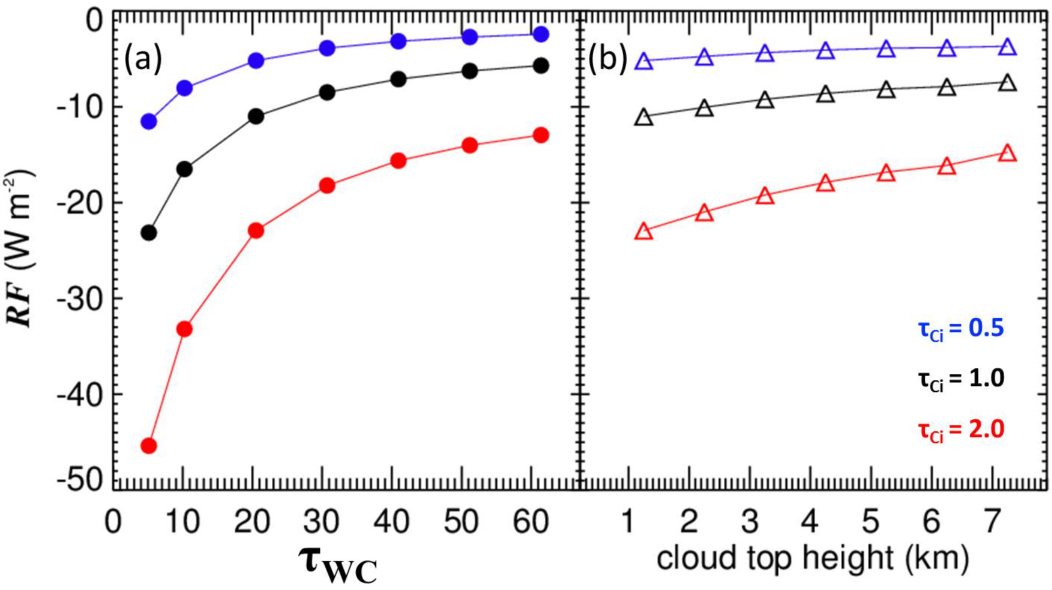

Figure 13. Integrated values of cirrus radiative forcing when a low water cloud is present. The optical thickness (left panel), and the top height (right panel) of the water cloud are varied. The colors indicate a different cirrus optical thickness.

Table 1. Shown are the optical thicknesses for a cirrus between 6.7 km and 8.5 km altitude assuming different ice crystal shapes for Approach I (constant number size distribution) and Approach II (constant ice water content).

	Approach I	Approach II
Droxtal	1.49	2.68
Solid Column	1.50	3.20
Column 8 Elements	0.77	7.45
Plate	1.15	4.44
Plate 10 Elements	0.54	15.4
Hollow Bullet Rosette	0.97	9.52
Baum	1.00	5.09